Inversion of structural geology data for fold geometry

L. Grose, Gautier Laurent, L. Ailleres, R. Armit, M. Jessell, T. Cousin-Dechenaud

JGR-Solid Earth, 2018
10.1029/2017jb015177

Inversion of structural geology data for fold geometry

L. Grose[1,*], G. Laurent[1,2], L. Aillères[1], R. Armit[1], M. Jessell[3], and T. Cousin-Dechenaud[2]

[1]*School of Earth, Atmosphere and Environment, Monash University PO Box 28E, Victoria, Australia*
[2]*Université de Lorraine, CNRS, Laboratoire GeoRessources, 54000, Nancy, France*
[3]*The University of Western Australia, Centre for Exploration Targeting, , School of Earth and Environment, Perth, Western Australia, Australia*
[*]*Corresponding author: lachlan.grose@monash.edu*

Highlights

- Structural modeling of folds is framed as an inverse problem
- Bayesian inference is used to find a range of possible fold geometries for a given dataset
- Data uncertainty is incorporated into the description of geological structures
- Variability between simulated models can be used to target further data collection

Abstract Recent developments in structural modeling techniques have dramatically increased the capability to incorporate fold related data into the modeling workflow. However, these techniques are lacking a mathematical framework for properly addressing structural uncertainties. Previous studies investigating structural uncertainties have focused on the sensitivity of the interpolator to perturbing the input data. These approaches do not incorporate conceptual uncertainty about the geological structures and interpolation process to the overall uncertainty estimate. In this work, we frame structural modeling as an inverse problem and use a Bayesian framework to reconcile structural parameters and data uncertainties. Bayesian inference is applied for determining the posterior probability distribution of fold parameters given a set of structural observations and prior distributions based on general geological knowledge and regional observations. This approach allows for an inversion of structural geology data, where each realisation can differ in the structural description of the fold geometries, instead of finding only a single best fit solution. We show that analysing the variability between the resulting models highlights uncertainties associated with the geometry of regional structures. These areas can be used to target where additional data would be most beneficial for improving the model quality and efficiently reducing structural uncertainty.

Keywords
Geological inversion
Structural modeling
Geological uncertainty
Inverse problem
Folding
Structural geology

1 Introduction

Three-dimensional geological models are a representation of the distribution of rock units and their structural relationships. They find practical applications throughout a wide range of geoscientific disciplines ranging from visualisation, interrogation, advanced analysis and process simulation. Three-dimensional models are usually more difficult to create than a geological map because they require the prediction of geological structures away from observations, usually at depth, which are difficult to constrain from surface observations and sparse drill hole datasets. There are a range of different approaches where modeling methods either: (1) almost exclusively use prior geological knowledge [*Jessell and Valenta*, 1996], (2) a hybrid approach where geological knowledge is incorporated by adding some kinematic information and combined with direct observations [*Moretti*, 2008; *Bigi et al.*, 2013; *Laurent et al.*, 2013, 2016], and (3) other systems only using observations in 3D space. A common method for building 3D models is to only consider observations to create an *explicit* representation of the surface by either interpolating between data points or triangulating a surface directly from the data [*Mallet*, 1992, 2002; *Caumon et al.*, 2009]. Another framework for representing these surfaces is to use an *implicit* representation of the surface [*Lajaunie et al.*, 1997; *Cowan et al.*, 2003; *Aug et al.*, 2005; *Frank et al.*, 2007; *Caumon et al.*, 2013; *Hillier et al.*, 2014] where the geological surface(s) are represented as iso-values of a volumetric scalar field. All of these approaches typically produce a single best fit model for the structural observations.

Depending on their geometry and dimension, folds have the potential to introduce dramatic complexity and uncertainty in the process of structural modeling. Even relatively gentle folded structures perturb the spatial correlation of structural observations. For this reason, folds remain a challenge for the interpolation schemes at the basis of implicit structural modeling. To constrain the geometry of folds, the geologist is generally required to draw fold profiles on cross sections or level maps, using bedding orientations [*Maxelon et al.*, 2009; *Jessell et al.*, 2010, 2014]. Additional foliations and lineations are generally overlooked and not directly used by the 3D interpolation algorithms used in 3D geological modeling. In particular, it is not trivial to input the structural information recorded from field studies such as fold axial traces and their structural elements (fold axes, fold vergence and fold overprinting) into the 3D interpolation algorithms [*Jessell et al.*, 2014]. *Laurent et al.* [2016] incorporate these additional structural datasets by modeling all foliations starting from the most recent, modeling each preceding event accounting for the geometry of the younger foliation. With this approach, folds are embedded into a fold frame that represents the structural elements of

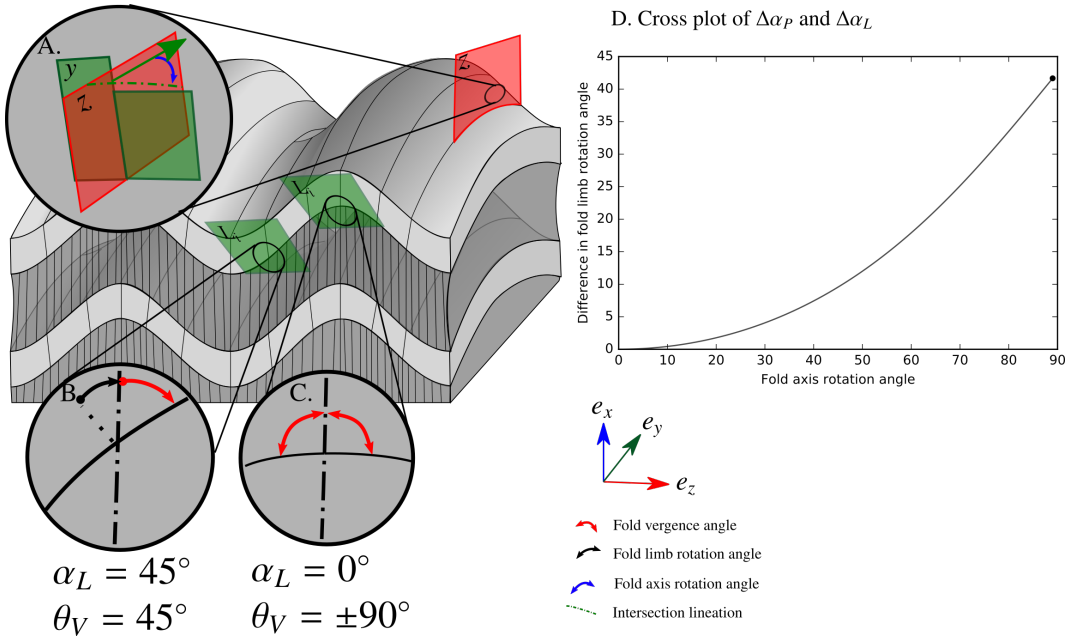

Figure 1 Schematic fold showing the fold axis rotation angle. (a) The fold limb rotation angle calculated in the plane normal to the fold axis. (b) and (c). (d) Cross plot showing the change in fold limb rotation angle α_L plotted against changes in the fold axis rotation angle α_P. Adapted from *Grose et al.* [2017].

the fold: axial surface, axis and vergence. The geometry of each folding event can be derived from the available structural data using geostatistical analysis within the fold frame [*Grose et al.*, 2017]. The fold geometry is characterised within the fold frame using the best fit Fourier series to the field observations using the maximum likelihood method. The characterisation of the fold geometry can be framed as an inverse problem where the aim is to determine the Fourier series model parameters representing the observations. Using the maximum likelihood approach and finding a single solution to an inverse problem is usually not sufficient due to the complex multidimensional parameter space [*Mosegaard and Tarantola*, 1995]. In general, an understanding of the associated uncertainty is usually required, for fold geometries the aim is to understand the distribution of possible fold shapes given the observed data and not to only find the single best-fit fold geometry.

Previous approaches for sampling structural uncertainties have focused on either perturbing the input data [e.g. *Jessell et al.*, 2010; *Lindsay et al.*, 2012; *Wellmann and Regenauer-Lieb*, 2012] or perturbing reference model surfaces [e.g. *Thore et al.*, 2002; *Tacher et al.*, 2006; *Suzuki et al.*, 2008]. Neither of these approaches incorporate the uncertainty in both the description of the geological structures and interpolation process. In this contribution, we use the modeling framework of *Laurent et al.* [2016] and introduce a probabilistic representation of the fold geometry. The fold geometry is represented using a Fourier series where parameters constraining the wavelength and fold shape are represented by probability density functions (PDF). The parameters representing the fold shape are given a prior distribution containing the information that is known about the parameter, independent of the model that is being fitted. The prior distributions are constrained by a combination of additional data analysis, geological knowledge, and valid parameter ranges. The joint posterior distribution for the combined parameters is sampled using a Markov Chain Monte Carlo (MCMC) sampler. Using this system data uncertainty is represented using an uninformed prior PDF (no information about the data uncertainty is included in the sampling). We demonstrate the inversion of structural geology data for characterising fold geometries using a Fourier series to represent the fold geometry [*Grose et al.*, 2017], first on a range of simple fold shapes in one dimension, and then on a more complicated synthetic 3D model representing doubly plunging parasitic folding.

2 Description and Modeling of Complex Fold Geometries

Laurent et al. [2016] introduce a global fold frame with three coordinates (x, y, and z) representing the structural elements of the fold. The z coordinate of the fold frame is constrained so that direction vector e_z is perpendicular to the observations of the axial foliation associated with the folding event and observations of the axial surface of the fold [*Laurent et al.*, 2016]. The y coordinate of the fold frame measures the distance along the axial surfaces and is constrained so that e_y and e_z are orthogonal and e_y aligns at best with the observations of the fold axis.

Two rotation angles representing the geometry of the fold axis and the fold shape can be calculated from structural data. In Figure 1a the fold axis rotation angle (α_P) is shown as the angle between e_y and the intersection lineation. The fold limb rotation angle (α_L) is the angle between the normal to the folded foliation and e_z (Figure 1b,c). Figure 1d shows that the difference in the calculated fold limb rotation angle is dependent on the orientation of the fold axis, or the fold axis rotation angle at that location. The S-Plot is a cross plot of a fold rotation angle and the scalar field representing the associated structural elements direction [*Grose et al.*, 2017]. A sample semi-variogram comparing the fold rotation angles in the fold coordinate system can be used to identify the main wavelength of folding. The S-Variogram [*Grose et al.*, 2017] also uses the fold frame coordinates to

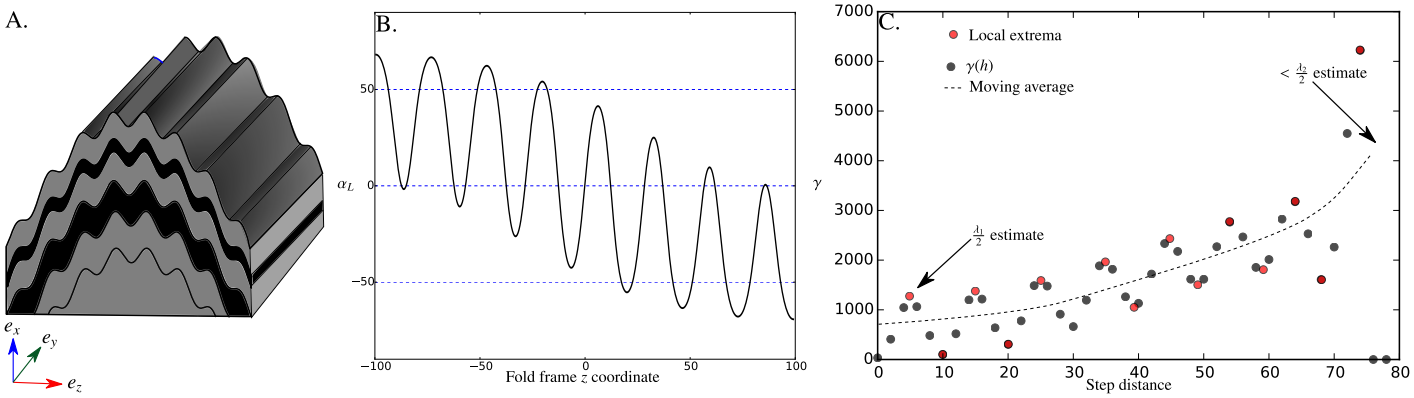

Figure 2 3D parasitic fold showing fold geostatitics and estimated wavelengths. (a) 3D diagram for multilayer parasitic folds, (b) S-Plot for parasitic folds shown in (a) and (c) the associated S-Variogram where black markers represent the variogram value for a particular step distance and red markers represent local extrema. The dashed curve represents the average trend of the extrema and would be constant for non-parasitic folding. The wavelength estimates are found by analysing these points. Figure modified from [*Grose et al.*, 2017].

analyse the fold rotation angles. The half wavelength of the fold can be automatically identified by finding the local maximum values of the S-Variogram [*Grose et al.*, 2017].

In *Laurent et al.* [2016], the fold shape is constrained by fitting an analytical fold profile that produces a periodical fold geometry. This allowed for the fold to be described by parameters that are comparable to the geometrical description of the fold used by structural geologists, e.g. the fold wavelength, tightness, and asymmetry. *Grose et al.* [2017] use a data-driven approach to interpolate the best-fit description of the fold based on the structural observations by smoothing and interpolating the observations before fitting a Fourier series. The local orientation of the fold axis is found by rotating e_y around e_z by the fold axis rotation angle (an angle between $-90°$ and $90°$). The orientation of the folded foliation is locally constrained by rotating the fold frame around the fold axis by the fold limb rotation angle.

3 A Probabilistic Framework for Modeling Fold Geometries

In both *Laurent et al.* [2016] and *Grose et al.* [2017], only a single best fit fold geometry is produced for a single data set. In practice, a single realisation of the fold geometry does not capture the uncertainty of the observations. The parameters representing the fold geometry, either in the form of an analytical profile [*Laurent et al.*, 2016] or the Fourier series parameters [*Grose et al.*, 2017], should be considered as random variables. In the following section, the Fourier series model parameters are represented using a probability density function (PDF), and modeling of the fold geometries is framed as a Bayesian inference problem.

3.1 Fourier series representation of fold geometry

The fold rotation angles ($\alpha_{P,L}$) are first transformed to gradients ranging from $(-\infty, \infty)$, using the transformation, $\hat{\alpha}_{P,L} = tan\ \alpha_{P,L}$ [*Grose et al.*, 2017]. The transformed fold rotation angles (fold gradients) can then be represented using a Fourier series, i.e. a linear combination of trigonometric basis functions.

Parasitic folds (Figure 2a) are very characteristic features of geological multilayer buckle folds. They typically share the same (or similar) fold axis and axial plane orientation as the larger fold, and a characteristic asymmetry (or fold vergence) [*Twiss*, 1992]. Parasitic fold asymmetry referred to as S and Z shape on either limb of the larger fold, and symmetric W or M shape close to the hinges of the larger fold [*Ramsay and Huber*, 1987; *Frehner and Schmalholz*, 2006]. The observed curve in the S-Plot will be a superposition of both fold wavelengths (Figure 2b) and needs to be captured in the interpolated fold rotation angle fields.

In *Grose et al.* [2017], fold wavelength is inferred by identifying the first local maximum for the S-Variogram. The first local maximum corresponds to the smallest wavelength captured by the structural observations. In most cases this will be the wavelength of parasitic folds (Figure 2). The scale of the identified wavelength depends on the minimal step size used for computing the S-Variogram. It is first computed with a step size 20% greater than the minimal distance between data points for identifying the smallest meaningful wavelength (λ_1). To identify larger wavelengths of the fold the most intuitive approach may be to use previously identified fold wavelength (λ_1) as the step size for a new S-Variogram and repeat the process. However, this will often identify wavelengths equal to multiples of the parasitic fold wavelength. Instead, we identify consecutive pairs of extrema (shown by the red dots in Figure 2c) and calculate the average value for the variogram using pairs of extrema. The average variogram values can then be analysed for any extrema. If there are multiple wavelengths of folds evident in the dataset then the moving average curve will show either a periodical trend or a general increase as the step distance increases. For an identified wavelength to be valid we apply the following criteria: (1) the variogram for the maximum must be greater than its neighbouring extrema by at least 5%, and (2) if a parasitic fold exists $\gamma(\lambda_2)$ for the larger fold must be 20% greater than $\gamma(\lambda_1)$ of the parasitic fold. These criteria allow for the number of wavelength scales N to be identified by the S-Variogram.

The transformed fold rotation angles are represented using the Fourier series:

$$\hat{\alpha}(x_i|A_0, A_{1\ldots n}, B_{1\ldots n}, \lambda_{1\ldots n}) = A_0 + \sum_{n=1}^{N} B_n \cos\frac{2\pi}{\lambda_n}x_i + \sum_{n=1}^{N} A_n \sin\frac{2\pi}{\lambda_n}x_i \quad (1)$$

where N is the number of wavelengths identified using the S-Variogram, x_i are the fold frame coordinate values, A_n and B_n are the Fourier series coefficients and λ_n corresponds to the different scale wavelengths. For brevity the parameters of the Fourier series will be defined as $\theta \equiv \{A_0, A_{1...n}, B_{1...n}, \lambda_{1...n}\}$ thus the deterministic model becomes $\hat{\alpha}(x_i \mid \theta)$.

3.2 Bayesian Inference

The fold axis and fold limb rotation angles can be represented using Equation 1. The parameters can be estimated using Linear Least Squares approach if the wavelength(s) λ_n are known [*Grose et al.*, 2017]. However, this assumes that the inferred wavelengths are the best representation of the fold geometry. *Grose et al.* [2017] show that the estimated wavelength is sensitive to data spacing meaning that additional tuning may be required. A non-linear approach, such as the Levenberg-Marquardt algorithm could be used if the wavelength values are unknown, though these methods typically assume that the model exactly represents the data and tries to optimise the parameters using this assumption.

Bayesian inference is a commonly used method for solving non-linear problems with extensive application in geosciences particularly in solving inverse problems in geophysics [e.g. *Kolb and Lekić*, 2014; *Muir and Tkalčić*, 2015; *Mosegaard and Tarantola*, 1995]. The main advantage of using Bayesian methods over standard statistical methods is in the ability to incorporate additional knowledge in the form of prior distributions. Bayesian inference uses Bayes' theorem to find the range in possible parameter values by combining the prior information (in this case, the range in possible fold geometries and predicted wavelength(s) using the S-Variogram) and data (in this case structural observations).

Bayes' theorem states that the posterior distribution of the model parameters is:

$$P(\theta \mid \alpha_i) = \frac{P\left(\alpha_i \mid \theta\right) \cdot P\left(\theta\right)}{P(\alpha_i)} \tag{2}$$

Where $P\left(\theta\right)$ is the prior probability of the parameters for Equation 1 and $P(\alpha_i)$ is the probability of the data and $P\left(\theta \mid \alpha_i\right)$ is the posterior probability of the parameters given the data. This can be simplified by taking the probability of the data as a normalisation term because the probability of the data is the same for all parameter values:

$$P(\theta \mid \alpha_i) \propto P(\alpha_i \mid \theta) \cdot P(\theta) \tag{3}$$

We assume that the structural observations are sampled from an unknown Gaussian distribution, a common assumption in previous work [*Wellmann and Regenauer-Lieb*, 2012; *de la Varga and Wellmann*, 2016] and other natural sciences where the underlying probability distributions are unknown. Hence, we use a Gaussian likelihood function:

$$P(x_i, \hat{\alpha}_i \mid \theta) = \frac{1}{\sqrt{2\pi\sigma^2}} \exp\left[-\frac{[\hat{\alpha}_i - \hat{\alpha}(x_i,\ \theta)]^2}{2\sigma^2}\right] \tag{4}$$

Previous studies have used $\sigma^2 = 5°$ [*Lindsay et al.*, 2012] or $\sigma = 10°$ [*Wellmann and Regenauer-Lieb*, 2012] for the structural uncertainties. In practice, the uncertainty associated with structural observations is unknown and is difficult to estimate robustly. Geological uncertainty can have a wide range of sources that have been broadly separated into three categories [*Cox*, 1982; *Mann*, 1993; *Bárdossy and Fodor*, 2001] and applied to structural geology [*Wellmann et al.*, 2010]:

- Type 1: data imprecision, error, and bias, e.g. the location of a contact or the orientation of the surface,
- Type 2: uncertainty related to the unpredictability and randomness in the interpolation, and
- Type 3: lack of knowledge about the structure being modeled, e.g. how representative are the observations of the geometry of the surface being modeled.

In practice, it is impossible to quantify the contributions of each source of uncertainty and as a result, it is impossible to objectively quantify the uncertainty associated with structural observations. When using structural observations to create a 3D model, or in this case characterise the fold geometry, we are actually interested in the combined misfit between the model and the structural observations, i.e. how closely do we expect the model to fit the data. Rather than adding further subjectivity into the modeling process, uncertainty of structural observations can be incorporated using a hierarchical Bayesian approach where the data uncertainty is represented by an additional probability density function, similar to *Muir and Tkalčić* [2015]. The misfit (σ) between the observed fold rotation angle and the model (Eq. 1) is represented using an uninformed hyperparameter, Jeffery's prior [*Sivia*, 1996]. This allows for the noise in the data to be properly accounted for without requiring subjective, and usually wrong, user input quantifying the uncertainty associated with the data. This technique has been applied extensively in the geophysical literature [e.g. *Bodin et al.*, 2012a,b; *Kolb and Lekić*, 2014; *Muir and Tkalčić*, 2015]. This is an improvement on *Grose et al.* [2017] where the data are smoothed using a radial basis interpolation scheme and no specific assumptions are made about the noise in the data.

The wavelength(s) ($\lambda_{1...n}$) can be represented by a truncated normal prior distribution with a fixed standard deviation of $\lambda/3$ where $\lambda > 0$. The choice of prior is not independent of the data which conflicts with the idea of a prior [*Raftery*, 1996]. However, we have defined these priors following the approach of *Raftery* [1996] and *Gelman et al.* [2008], where the prior is chosen to capture "the broad possible range of the variable" in this case resulting from the large standard deviation. This approach results in priors that would be similar to priors generated by a person with relatively little existing knowledge [*Raftery*, 1996]. This is necessary to make the fold modeling process automatic without requiring any user-defined parameters. Alternatively the prior could be defined by geological knowledge, however, it is unlikely that the geologist would define this prior without considering the structural observations.

The prior distribution for the Fourier coefficients are each represented by Gaussian distributions with a mean of 0 and a standard deviation of 5. These weakly informative prior distribution for the coefficients cover the range of common fold geometries. As Equation 1 represents the gradient of the fold shape, the coefficients do not depend on the scale of folding. This means that the same priors can be used for all scales of folding.

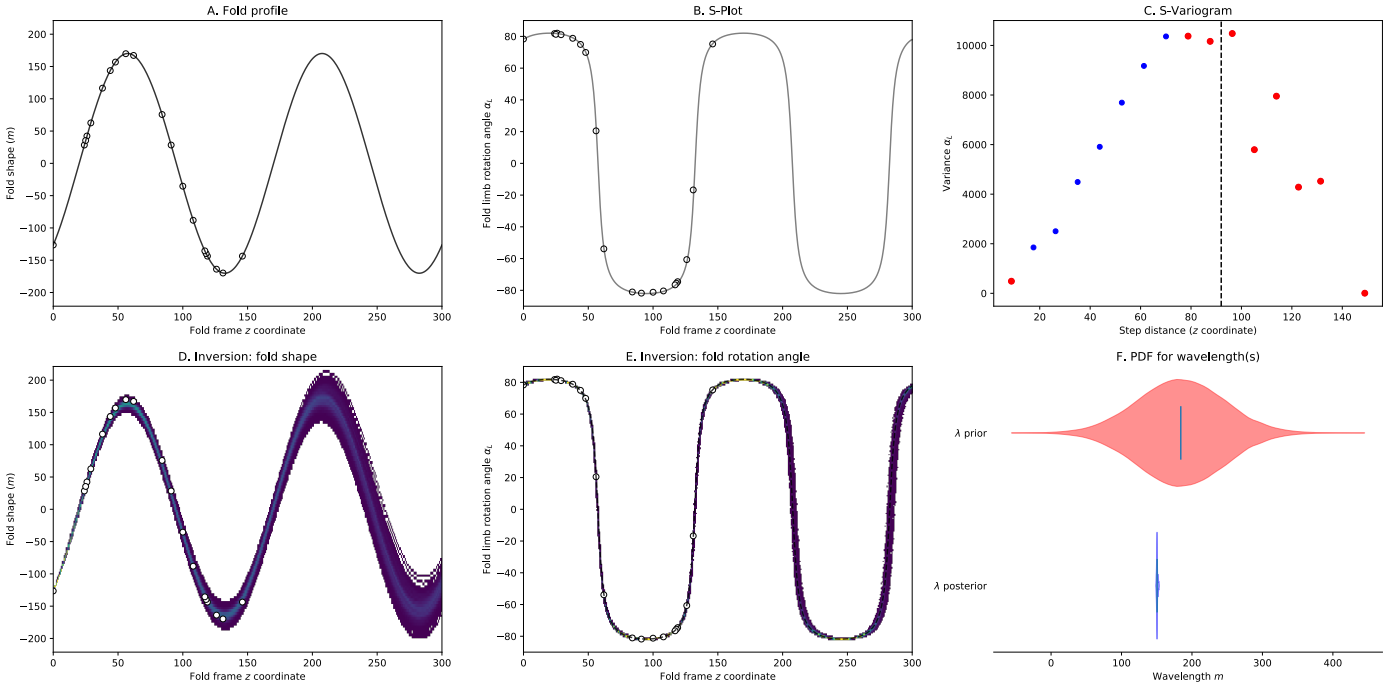

Figure 3 Proof of concept 1-D example for a sinusoidal fold geometry. (a) Reference fold shape with a fold wavelength of 150m and sample locations. (b) Reference fold profile and sample locations representing the fold rotation angle for the fold geometry in (a). (c) S-Variogram for the structural observations (blue dots in (a) and (b). The dots represent the variogram for all points at the corresponding step size. The red dots are the locations identified as being local extrema. The estimated half wavelength is shown by the dashed line. (d) Interpolated fold shape probability showing the range of solutions sampled with MCMC. (e) Fold rotation angle profile probability sampled from the posterior using MCMC. (f) Violin plot showing prior distribution and 1-D slices of theposterior distributions for the fold wavelength.

3.3 Sampling from the Posterior Distribution

The probabilistic representation of the fold geometry is incorporated into the fold modeling workflow [*Laurent et al.*, 2016; *Grose et al.*, 2017] to represent both the fold axis (α_P) and the fold limb (α_L) rotation angles. Each rotation angle is represented throughout the model volume within the fold frame coordinates using two Fourier series (Equation 1). The joint posterior distribution is approximated using the information provided by two Gaussian likelihood functions and the prior probabilities. The first likelihood function $P(L_i,\ F_i \mid \theta_P, \sigma_P)$, characterises the α_P for the fold axis rotation angle calculated for observations of the intersection lineation or fold axis observations and the fold frame given the fold axis rotation angle parameters (θ_P). The second likelihood function $P(S_i,\ F_i|\ \theta_P,\ \theta_L,\ \sigma_L)$ characterises the modeled fold limb rotation angle α_L given the observed folded foliation S_i. The calculated fold limb rotation angle depends on the current fold axis orientation (Figure 1) that can be calculated using the fold frame F_i and the parameters representing the fold axis θ_P. The misfit between the modeled fold rotation angles and observations are represented by Jeffery's prior [*Sivia*, 1996]: This process is applied within the fold frame coordinates for the current folding event and could be applied to multiple deformation events where the most recent foliation is modeled first.

The joint posterior distribution $(P(\theta_P,\theta_L,\sigma_P,\sigma_L,F_i\ |L_i,S_i)$ is sampled using a Markov Chain Monte Carlo (MCMC) sampler implemented in PyMC2 [*Patil et al.*, 2010]. This implementation uses the adaptive Metropolis-Hastings step method to tune the parameters to their optimal values. The sampler is run using a "burn in" period to condition the parameter values. Each sample location in the joint posterior distribution contains the parameters to characterise the fold rotation angles throughout the model volume. A realisation of the 3D geometry can be generated for each sample location using the fold constraints from *Laurent et al.* [2016]. In this study we investigate the effect of changing the description of fold geometries on the resulting 3D models and do not consider additional interpolation parameters such as mesh resolution or choice of interpolation algorithm on the interpolation results.

4 Case Studies

4.1 Proof of Concept

Figure 3a is a symmetrical fold shape generated from a sine wave with a wavelength of $150m$. The folded layer has been randomly sampled within a single fold wavelength capturing synformal and antiformal hinge zones. The sample locations are represented by the white dots in Figure 3a. The S-Plot for the fold shape in (a) is shown in Figure 3b and the calculated fold rotation angle for the structural observations in (a) are illustrated by the white dots. Figure 3c shows the S-Variogram where the step distance is chosen to be equal to the average nearest neighbour distance between the observations. Local maxima and minima (red dots) are identified in the resulting curve using the gradient descent method [*Cauchy*, 1847]. Each pair of extrema is analysed to determine whether it represents a fold wavelength (e.g. multiscale folding) or if it is just capturing noise in the dataset. In this example, no small wavelength folding exists and the identified extrema are interpolated into a smooth curve and this is analysed to find the main fold wavelength. In this case, a peak of $82m$ (Figure 3c) relates

to folding with a wavelength of about $164m$.

The structural observations are inverted by sampling from the joint posterior distribution, $P(\theta, \sigma, x_i|\alpha_i)$ using the MCMC sampler. The sampler was run for $10,000$ iterations and a burn in period of $5,000$ iterations were discarded. The profile in Figure 3d shows the fold geometry interpolated using the observations and fold constraints from the S-Plot (Figure 3e). In both Figures 3d,e the colour map represents the range of possible fold profiles from the joint posterior distribution. Figure 3f shows the posterior and prior distribution for λ_1. The wavelength in this example is well constrained with a narrow estimated PDF capturing the reference fold wavelength of $150m$.

A more complicated fold shape is shown in Figure 4a where an additional fold with a wavelength of $15m$ has been superimposed on the reference fold from Figure 3. This model has also been sampled capturing one full wavelength of the larger scale fold. Figure 4b is the S-Plot for the reference fold shape showing the sample locations. The S-Plot plots the fold rotation angle that is representative of the slope of the fold shape and easily picks out the smaller scale parasitic folds. The large scale fold can be seen by the change in average fold rotation angle for each parasitic fold hinge. Figure 4c shows an S-Variogram for the observations in b. Each dot represents the variogram value for pairs separated by the step distance and the red dots also represent the points identified as extrema. A local maximum can be seen at approximately $23m$ and this has a significantly higher variogram value than the surrounding extrema and can be interpreted to represent a fold wavelength of approximately $46m$. The extrema (red dots) are interpolated into a smooth curve and the local maxima of this curve is identified to be approximately $83.5m$ suggesting a wavelength of $167m$ for the larger wavelength fold. For both Figures 4d and e, the scaled colour map represents the joint posterior distribution sampled using MCMC. In Figure 4f, the prior and posterior distributions for λ_1 and λ_2 are shown. The red polygons show the prior PDFs and the blue polygons show the posterior PDFs. The posterior distribution for the parasitic fold (λ_1) has a mean of 15 and a standard deviation of < 1 suggesting that the data constrains the smaller scale wavelength very well. The posterior for the main fold (λ_2) is similarly well defined with a slightly larger standard deviation.

4.2 Parasitic Non-Cylindrical Folding

In the final example, we demonstrate the application of these techniques to a 3D example where structural observations are inverted for the fold geometry. The reference model was generated using Noddy [*Jessell and Valenta*, 1996] using the python interface, pynoddy [*Wellmann et al.*, 2016]. The models consists of a doubly plunging parasitic fold generated by superimposing a fold with a wavelength of $8,000m$ and an amplitude of $1,500m$ with another fold with a wavelength of $1,000m$ and amplitude of $500m$, the axial surfaces for the two folding events are parallel $N000/90$. To create the doubly plunging effect an additional folding event with an axial surface dipping at $72°$ to the north striking perpendicular to the existing folds was used with a wavelength of $14,444m$ and amplitude of $1,000m$. The model was sampled from a synthetic topographical section. Observations constraining the orientation of the folded foliation, intersection lineation and contact location are shown in Figure 5. The structural observations for bedding and the fold axis have been perturbed to simulate uncertainty in the obser-

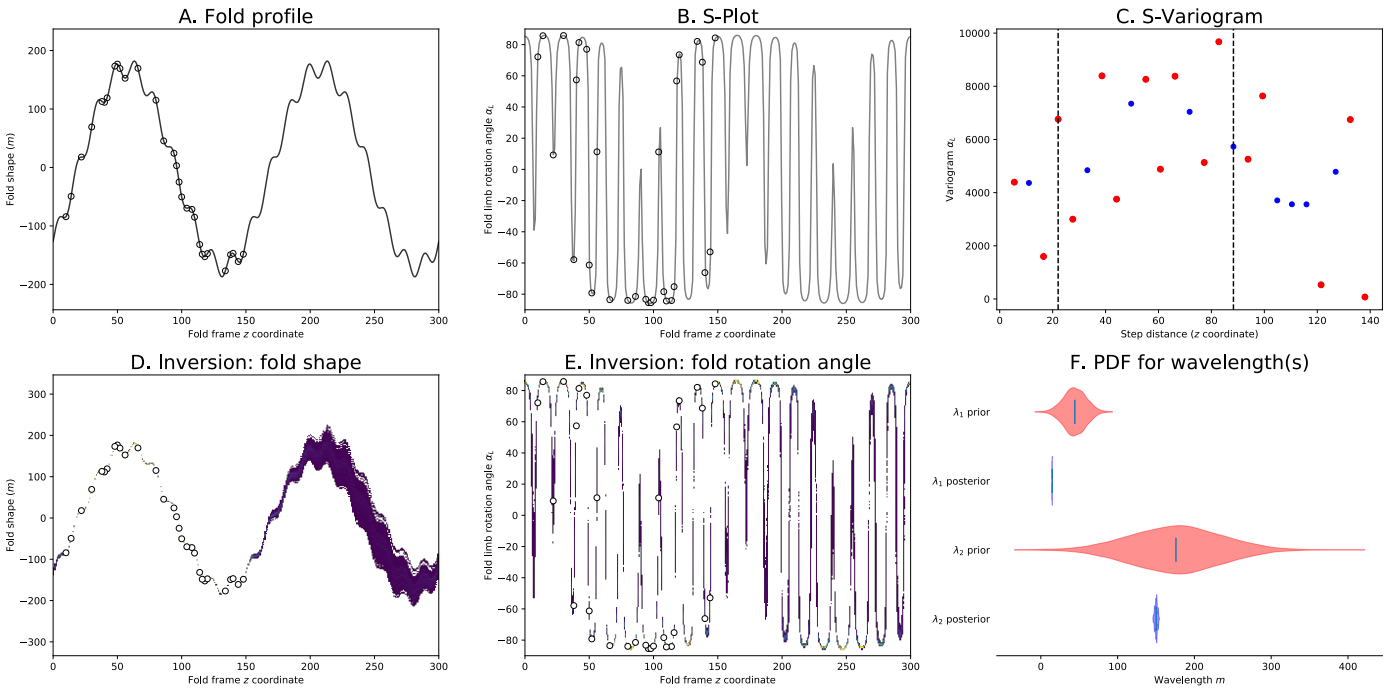

Figure 4 Proof of concept 1-D example for parasitic fold geometry. (a) Reference fold shape: $\lambda_1 = 15m$ and $\lambda_2 = 150m$ and sampling locations (b) S-Plot showing fold rotation angle for the fold in (a). (c) S-Variogram for the structural observations, white dots in (a) and (b). The dots represent the variance for all points at the corresponding step size. The red dots are the locations identified as being local extrema. The two estimated half-wavelengths are shown by dashed lines. (d) Interpolated fold profile probability sampled using the MCMC sampler.(e) Interpolated fold rotation angle probability modeled using the MCMC sampler. (f) Violin plot showing prior distribution and the slices of the posterior distribution for λ_1 and λ_2.

vations by sampling from Gaussian distributions describing the azimuth and plunge of the normal vectors with a standard deviation of $10°$.

The fold frame for F_1 is constructed by first modeling the axial foliation of the fold using the observations for S_1 to constrain the gradient of z coordinate, e_z (see Figure 1). The fold axis direction field y is interpolated so that $e_z \cdot e_y = 0$, this enforces the geological constraint that the fold axis must be a line within the axial foliation surface. We choose an arbitrary direction of $e_y = e_z \times (0\,0\,1)$ to make the resulting field unique. The fold axis direction field could also be interpolated using the average fold axis orientation. The differences between these fold profiles would be captured by the first term in the Fourier series (A_0) which controls the shift in the Y axis.

The fold axis rotation angle (α_P) is calculated by finding the angle between the local observation of the fold axis (either intersection lineation or direct observation of the fold axis) and the local orientation of the fold axis direction. This is plotted against the value of the y coordinate shown in Figure 6a. The S-Variogram (Figure 6c) appears to have a range of approximately $6,000m$. There is insufficient data to determine whether the range corresponds to the true half wavelength of the fold or only the sampling extent. It does provide enough information for the weakly informative prior distribution for the wavelength parameter of $N(12000, 4000)$. The fold limb rotation angle (α_L) is calculated using the local intersection lineation between the observations and the fold frame z coordinate (Figure 6b). This calculation of α_L is used to define the prior distributions for the fold parameters. Two wavelengths are identified using the S-Variogram (Figure 6d). The smaller wavelength results in regular periodicity in the S-Variogram and the first maxima is found at $500m$ which correlates with a wavelength of $1,000m$. The next wavelength is identified by the global maxima for the S-Variogram, in this case $5,500m$ and correlates with a fold wavelength of $11,000m$ (Figure 6d). Both the parasitic fold (λ_1) and main folding (λ_2) are represented by normal priors where the mean is the wavelength identified by the S-Variogram and the standard deviation is one third of the mean. All Fourier coefficients (for α_L and α_P) are represented by Gaussian prior distributions $N(0, 5)$.

The geological map (Figure 5) is inverted to find the joint posterior distribution $\left(P(\theta_L,\ \theta_P,\ \sigma_P,\ \sigma_L,\ F_i \mid S_i,\ L_i)\right)$ for the fold geometry. Each sample of the posterior distribution define interpolation constraints for the implicit folding algorithm [*Laurent et al.*, 2016; *Grose et al.*, 2017]. Two hundred model realisations (Figure 6e and f) are generated by sampling parameter values from the joint posterior distribution to inform the fold interpolation constraints. Figure 7 shows a random subsample of these models and the corresponding α_P and α_L curves. All models honour the structural style of the reference model showing two large scale fold hinges with parasitic folds occurring on the limbs. It is difficult to quantify the variability between models by visual inspection. Previous studies quantifying geological uncertainty in model simulations have used variability between the observed stratigraphy at unique locations throughout the model suite [*Lindsay et al.*, 2012; *Wellmann et al.*, 2010; *Wellmann and Regenauer-Lieb*, 2012]. *Wellmann and Regenauer-Lieb* [2012] use information entropy as a measure for variability in geological model iterations. In their work, the information entropy was calculated on the stratigraphic unit occurrences. In this study, we will adapt the concept of information entropy to the interpolated scalar field value because we are only interested in the geometrical variability between model suites not limited to the resolution of the chosen stratigraphy. Information entropy using the method from *Wellmann and Regenauer-Lieb* [2012], however instead of using the probability of the stratigraphic units we assess the probability of 10 equally sized intervals dividing the scalar field range. This is equivalent to dividing the stratigraphic column into equal thickness units. The number of intervals can be varied to increase or decrease the resolution of the uncertainty.

Another method to identify regions of structural variability, e.g. location of fold hinges and the geometry of the fold axis, is to compare the orientation of the interpolated surfaces between model suites. The orientation variability can be defined as:

$$V = \frac{1}{N} \sum_{i=1}^{N} cos\left(n_i \cdot n_{av}\right) \tag{5}$$

where V is the local variability value (in degrees), N is the total number of model iterations, n_i is the normal vector representing the local orientation of the surface for model i and n_{av} is the mean orientation of all interpolated surfaces for this location in the model. The calculated value of V represents the standard deviation of the distribution of orientations for the particular tetrahedron from the interpolation mesh and as a result is a good proxy for geological uncertainty. A higher value for V indicates more variability in the orientation of the surface and can be used as a proxy for structural uncertainty at that location in the model suite.

Figures 8a and b shows the information entropy for the model volume and the reference model surfaces. In Figures 8c and d, the angle variability is used as a proxy for geological uncertainty. Both information entropy and angle variability show an increase in geological uncertainty in the western region of the model. The angle variability (Figure 8c) shows a periodical trend of high and low variability across the model suite from east to west. The areas of high variability are associated with fold hinges in the reference model with increasing variability where the wavelength of the main fold is not constrained. The regions of lowest variability are associated with locations where there is a higher density of structural data. The locations where the scalar field values are constrained by control points are evident in the circular features in Figure 8a.

The regions of higher variability highlighted in Figure 8 can also be observed in Figure 6f where there is more variability in the interpolated profiles between -4000 and 0 in the z coordinate, which correlates with the western portion of the model. The geometry of the parasitic folds are well constrained in Figure 6f where the posterior distribution has a relatively small standard deviation of $5m$. The main fold wavelength is not as well defined and has a standard deviation of $300m$. This variation in the posterior for the larger wavelength is a major contribution to the variability increasing away from the main data locations in the north east of the model.

In Figure 6e there is high variability between the fold axis rotation angle profiles. The range in profiles can be up to $20°$. However, in the variability models (Figure 8) this is is

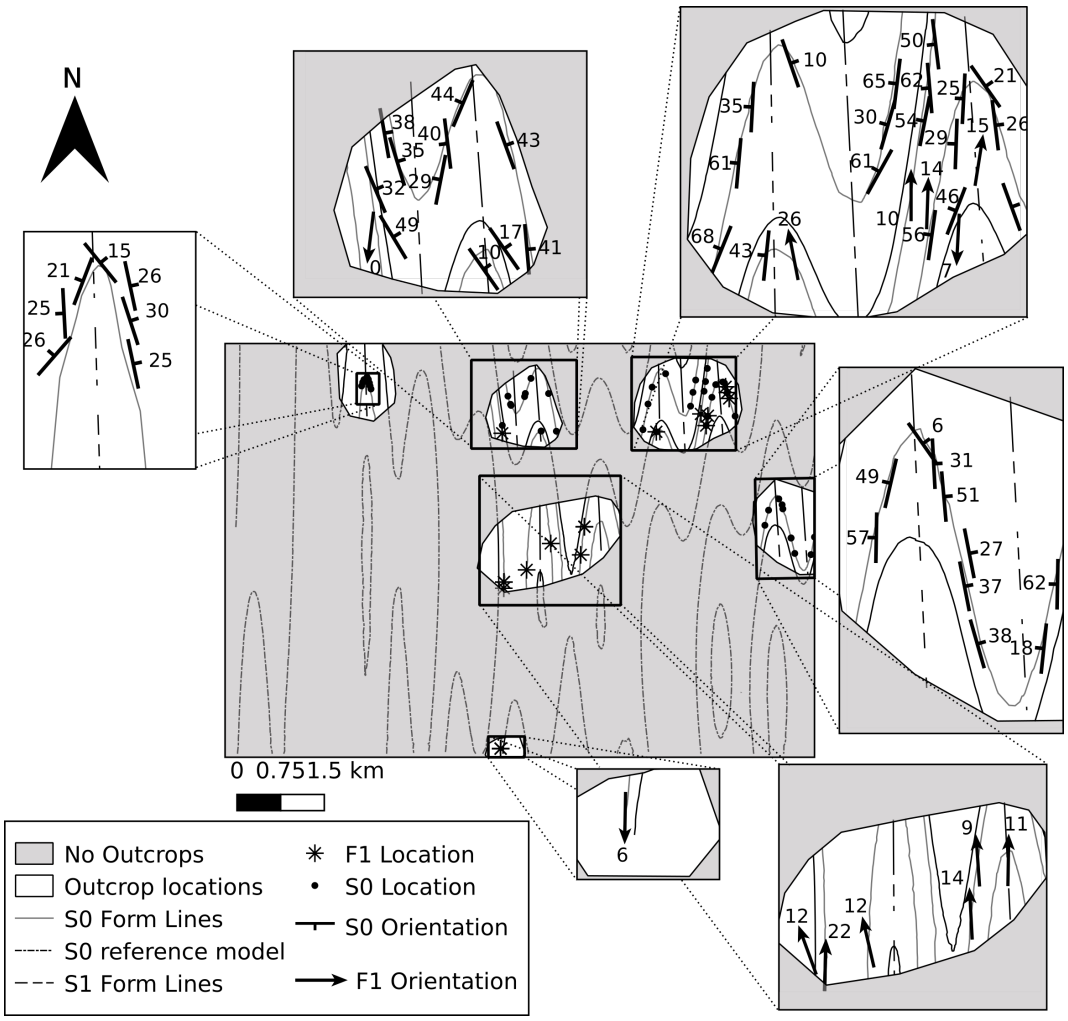

Figure 5 Synthetic topographical surface showing form lines representing bedding surface traces and location of orientation data points sampled from the reference model.

not evident. A subtle trend can be observed along the fold axes in the information entropy Figure 8a and in the eastern region of the model in Figure 8c where the angle variability slightly increases in the north and south areas of the model. There are three reasons why the fold axis rotation angle does not contribute to model variability as signifciantly as the fold limb rotation angle: (1) In this model, the fold axis is only gently doubly plunging, with a maximum of $50°$ of variation between observations compared to up to $100°$ for the fold limb rotation angle; (2) in the western region of the model the contribution of the larger wavelength shifts the location of parasitic fold hinges and may cause variations in the orientation of the folded surface of up to $100°$ and; (3) the variation in fold axis is partially accounted for when the fold limb rotation angles are recalculated for each iteration of the fold axis due to the joint inversion of both angles.

In Figure 8 the variability increases away from geological observations. The posterior distribution for the larger wavelengh fold has a significantly higher standard deviation compared with the smaller parasitic fold posterior distribution. In order to reduce model variability, more data is needed to constrain the wavelength of the main fold. Figure 9 shows a comparison between the variability models for the original dataset (a and c) and a new model suite where additional orientation data has been sampled (b and d). The orientation data constrains the geometry of an additional parasitic fold hinge at the location of highest variability (indicated in Figures 9a,c). These additional orientation observations reduce the higher variability trend in the western portion of the models. Most of the variability in the updated model suite is associated with the location of the fold hinges and the geometry of the fold axis. The uncertainty associated with the main fold geometry has been significantly reduced. The standard deviation for the wavelength posterior has been reduced by 68%. There are locations that exhibit localised high angle variability and low information entropy. These areeas are associated with the locations for value control points that are collocated with the fold axis observations. This is because all model realisations are enforced to have very similar scalar field values at these locations. Varying fold models are thus accounted for by significant orientation variations at these locations. These are modeling artifacts resulting from the interpolation method. These artifacts could be reduced if value constraints, that in a geological sense only identify the stratigraphic unit and not the distance from contact locations, are implemented as inequality constraints [*Frank et al.*, 2007; *Hillier et al.*, 2014] or by using the iterative methods proposed by *Collon et al.* [2016]. Inequality constraints define boundary values (e.g. the range for a particular stratigraphic unit) to the model instead of forcing a scalar field value at that location. This would result in less significant variability in the interpolated geometries.

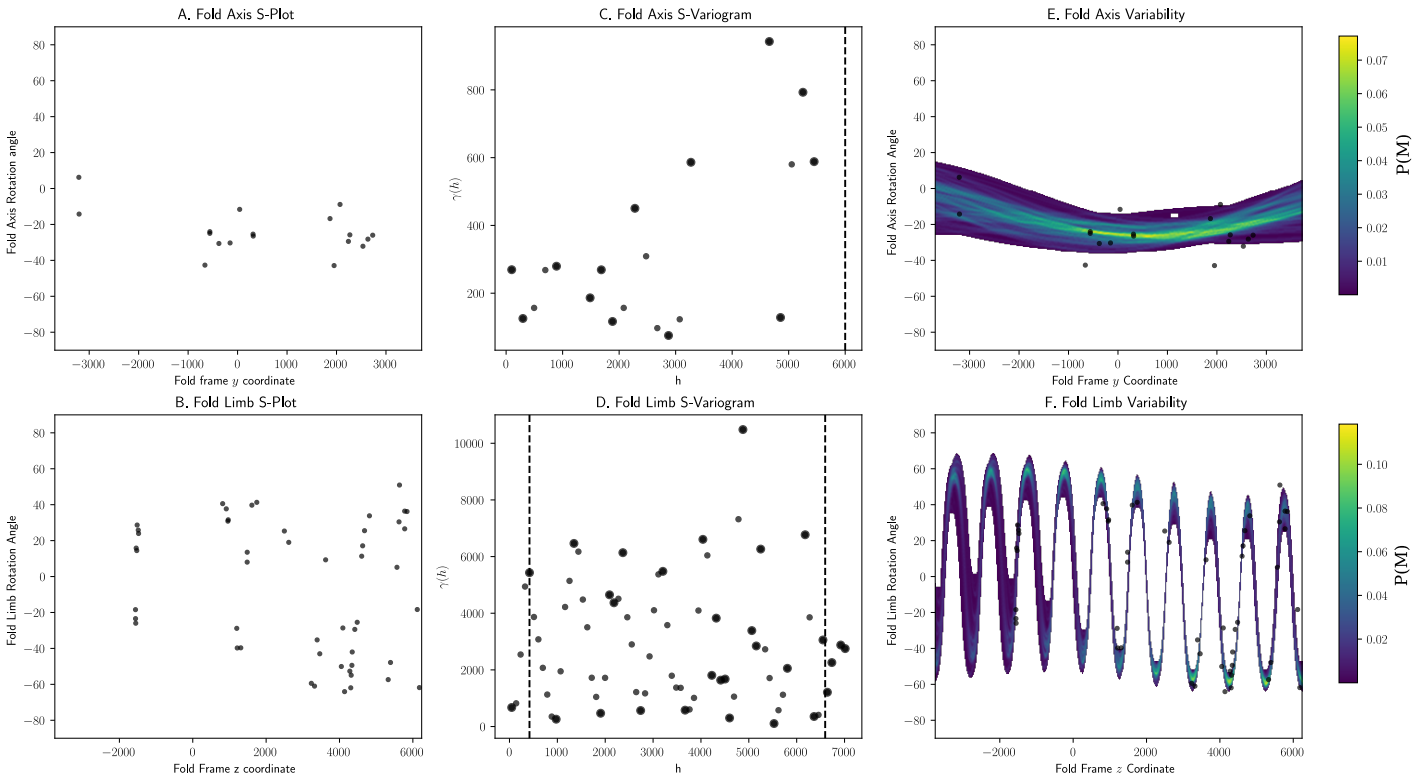

Figure 6 Fold geostatistics and Bayesian inference results for synthetic example. (a) S-Plot of α_P and y coordinate. (b) S-Plot α_L and z coordianate. (c) S-Variogram of α_P, dashed vertical line represents the location of $\frac{\lambda}{2}$. (d) S-Variogram of α_L, dashed vertical lines represents the location of $\frac{\lambda_N}{2}$. The fold profiles sampled from the joint posterior distribution are shown in (e) (α_P) and (f) (α_L). Where P(M) is the probability of α_L or α_P for the fold frame coordinates.

5 Discussion

Geological modeling has previously been considered as an inverse problem [e.g. *Wood and Curtis*, 2004; *Aydin and Caers*, 2017; *de la Varga and Wellmann*, 2016; *Wellmann et al.*, 2017]. In these approaches the structural data represents the prior geological knowledge, or model parameters ($P(\theta)$) and the data ($P(D)$) is usually not the structural datasets used to create geological models. For example, *Aydin and Caers* [2017] introduce a likelihood function that represents the mismatch between fault observations (seismic interpretations) where the priors are the strike and dip from analog areas. *Wellmann et al.* [2017] and *de la Varga and Wellmann* [2016] use geology-based likelihood functions that characterise geological and geophysical observations such as: fault geometry, probability of folding, probability of a discontinuity, the probability of an unconformity or, potential field responses where the model parameters (prior knowledge) includes the structural observations. These approaches are suitable for faults where the orientation of the fault plane is a key description of the fault geometry. However, for folded surfaces the local orientation of the surface does not describe the fold geometry [*Grose et al.*, 2017]. In this contribution we have framed geological modeling of folds as an inverse problem and demonstrated that using the appropriate geometrical description of geological structures it is possible to invert geological data for 3D geometry.

Grose et al. [2017] use the wavelength parameter estimated from the S-Variogram as a fixed constraint for the fold wavelength and solve the Fourier coefficients using least squares regression. The quality of the resulting fold profiles is dependent on the wavelength estimated from the S-Variogram. In some cases, it may not be possible to exactly pick the fold wavelength from the S-Variogram, resulting in a poor fit and/or unlikely model geometries. For example, in the parasitic non-cylindrical fold model (Figure 6) the mean of the prior distribution is the estimated wavelength using the S-Variogram. Where the wavelength is well characterised by the structural observations, the estimated mean and the mean of the posterior distribution are very close. Where the folds are not as well characterised by the data, e.g. the larger wavelength fold, the estimated mean is outside of one standard deviation from the posterior mean. This suggests that the wavelength estimated from the S-Variogram is not the best representation for that fold. The posterior in this example has a large standard deviation suggesting that the data does not contain enough information to define a single wavelength value. If only a single model is produced and no uncertainty is associated with the different geometrical attributes, it would be difficult to predict the location and type of data that should be collected to reduce model uncertainty. When the posterior distribution for the fold geometries is sampled it is much easier to isolate the particular aspects of the fold geometry that are uncertain (e.g. in the synthetic case study more data constraining the large wavelength fold reduced model uncertainty).

The choice of prior distributions controls the search area (in parameter space) where parameter estimates can be drawn from. If the prior distributions are too restrictive then the resulting parameter estimates may not be able to represent the data. If the priors are too broad then the sampler may require a large number of iterations or may not converge. The choice of prior distributions is an important aspect in Bayesian statistics. In this study we have chosen

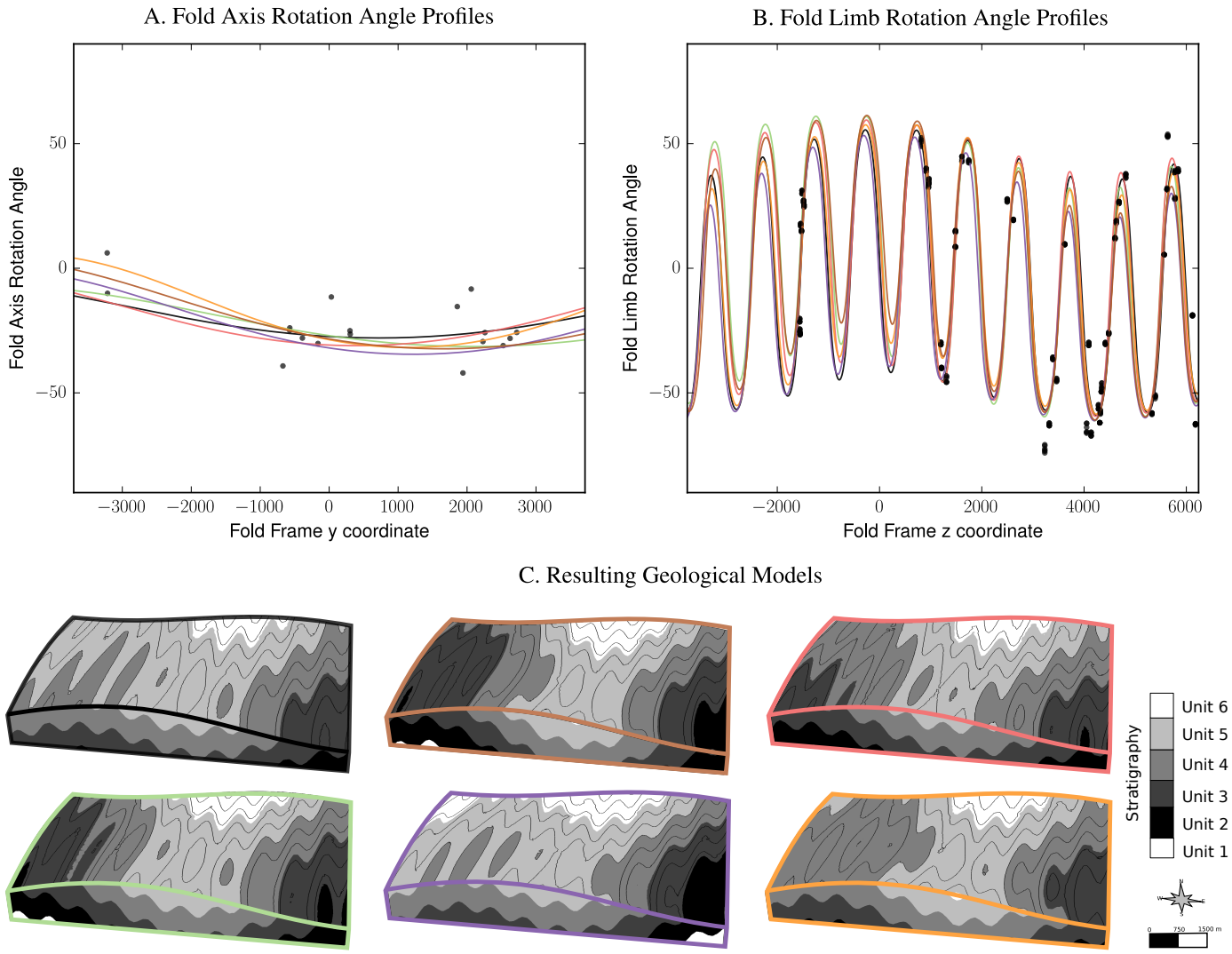

Figure 7 Six randomly selected models from model suite of 200 realisations showing: (a) fold axis rotation angle profile, (b) fold limb rotation profile, and (c) the resulting geological models.

to use weakly informative prior distributions that are based on, where possible, empirical estimates for the parameter values from the geological data. While the chosen prior distributions are quite broad they allow for the model to be supported by data. However, in some cases there may not be enough data for the joint posterior distribution to converge. There may be additional information that cannot be directly incorporated into the model using standard observations, such as fold wavelengths from outside of the map area, from geophysical data sets, or geological knowledge. In these cases, the relevant prior distributions could be made to be more informative. An alternative approach would be to incorporate these additional observations using an additional likelihood function. For example, *de la Varga and Wellmann* [2016] use multiple likelihood functions to incorporate additional geological knowledge such as fault offset and layer thickness that cannot normally be incorporated into the geological modeling system.

Most case studies where 3D models have been used to investigate geological phenomena have not incorporated parasitic folding into either the construction or the geometry of the geological model [e.g. *Maxelon et al.*, 2009; *Vollgger et al.*, 2015; *Basson et al.*, 2016]. This is mainly because using a standard modeling workflow the geometry of these folds would need to be defined manually by the user gleaned from either interpretive cross sections or synthetic data to constrain the resulting geometries. This process would be time consuming, subjective and probably not aid in interpreting the geology. Generally parasitic folds do not significantly affect the resulting large scale 3D geometries and are ignored during modeling. This approach is not consistent with field studies where parasitic folds are often used by the structural geologists to understand larger scale fold geometries and overprinting relationships [e.g. *Forbes and Betts*, 2004; *Armit et al.*, 2012; *Basson et al.*, 2016; *Tian et al.*, 2016]. Another consideration is that parasitic folds will affect the spatial correlation between structural observations (e.g. if structural data is collected from opposing limbs of a parasitic fold, out of context, this information may misinform the large scale model). By inverting structural data it is possible to identify both the larger scale geometry and the parasitic fold geometry as demonstrated in Figure 4. This means that models can be created that extrapolate the geometry of parasitic folds even where structural observations have not been recorded. An alternative approach would be to remove the parasitic folds from the model by identifying which structural observations are associated with the short limb and hinges of parasitic folds. Both of these approaches incorporate the information provided by the parasitic folds into the resulting model description.

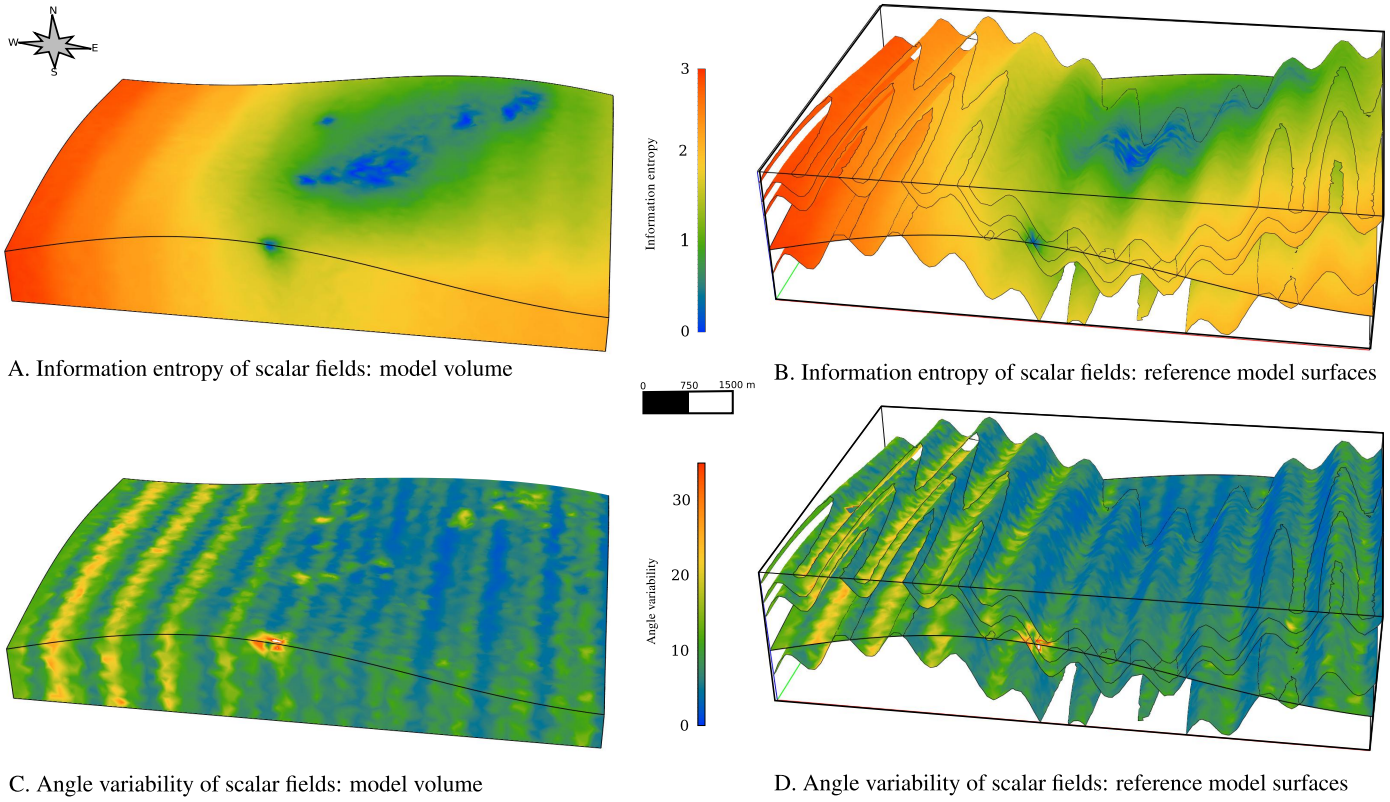

Figure 8 Model variability for simulation of 200 models. (a) and (b) information entropy used as a proxy for model variability, higher values indicates higher variability between models. (c) and (d) angle variability between interpolated models

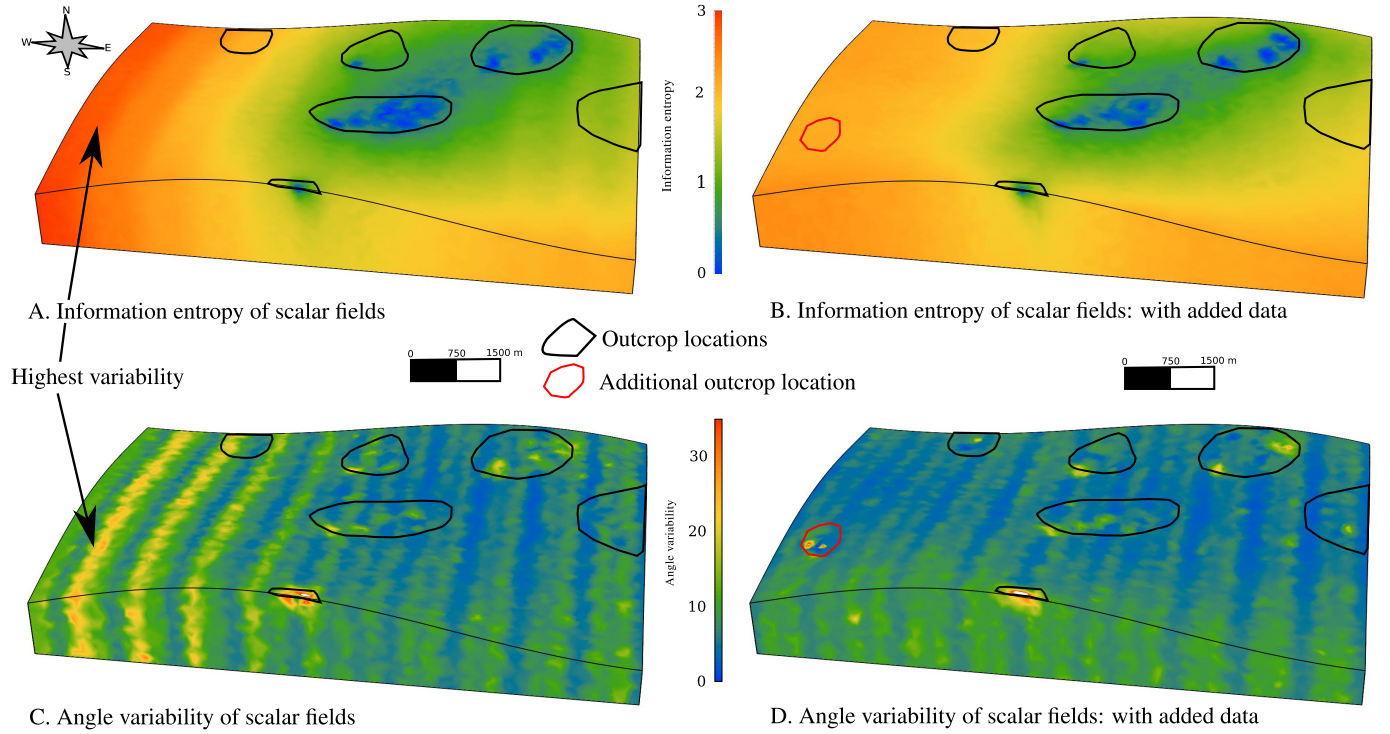

Figure 9 Comparison of model variability before and after adding additional data in the most variable location. (a): Information entropy calculated on interpolated scalar field for 200 model iterations using data in Figure 5. (b) Information entropy calculated on interpolated scalar field for 200 model iterations with additional data (c) Angle variability calculated on interpolated scalar field for 200 model iterations using data in Figure 5. (d) Angle variability calculated on interpolated scalar field for 200 model iterations with additional data. Outcrop locations are outlined in black and the additional outcrop location is outlined in red.

A focus for geological modeling research has been accounting for uncertainties in geological models [e.g. *Suzuki et al.*, 2008; *Cherpeau et al.*, 2010; *Jessell et al.*, 2010; *Wellmann et al.*, 2010; *Cherpeau et al.*, 2012; *Lindsay et al.*, 2012; *Wellmann and Regenauer-Lieb*, 2012; *Lindsay et al.*, 2013; *de la Varga and Wellmann*, 2016; *Thiele et al.*, 2016]. In these studies multiple realisations of the geological model are generated by perturbing the original structural data set

or existing model geometry. These studies have had two main caveats: (1) the difficulty for structural interpolation methods to generate realistic geological models from an input dataset particularly in polydeformed terranes [*Jessell et al.*, 2014], and (2) the uncertainty has only been considered associated with the structural observations rather than being associated with the interpolation method [*Aug et al.*, 2005]. To overcome the first caveat the geologist has been forced to constrain areas of the models using interpretive constraints [*Caumon et al.*, 2009] that can be subjective and can introduce additional human bias [*Bond et al.*, 2007]. In previous methods most of the simulated structural uncertainty has been associated with fault geometries [e.g. *Wellmann et al.*, 2010; *Lindsay et al.*, 2012; *Wellmann and Regenauer-Lieb*, 2012; *de la Varga and Wellmann*, 2016]. Folds have typically been difficult to model using implicit approaches because the interpolation algorithms generally fit the smoothest surface to the resulting model and folds generally create regular patterns of localised curvature variation. For this reason when the structural observations are perturbed [*Wellmann et al.*, 2010; *Lindsay et al.*, 2012; *Wellmann and Regenauer-Lieb*, 2012; *de la Varga and Wellmann*, 2016] the interpolation algorithm will in most cases smooth the introduced perturbations and the resulting model variability will not reflect the uncertainty in the geological structures. We have presented a method for simulating structural uncertainty where no assumptions about the representivity of the data is needed. The misfit between the model and the observations is incorporated into the probabilistic framework using the uninformative prior distribution. This results in the variability between inversion realisations being closely related to the geometry of the structures (e.g. Figure 8). In contrast, if uncertainty is simulated by perturbing the structural data and the same interpolation is used, the resulting models will have increased uncertainty only in the locations where the model is constrained.

6 Conclusion

In this contribution a new method for inverting geological data for fold geometries is presented. Folds are represented using the Fourier series description of fold geometry introduced in *Grose et al.* [2017] and the fold modeling framework of *Laurent et al.* [2016]. The probabilistic representation of the fold geometry offers improvements in finding the best fit fold geometry for a structural dataset, a new approach to simulating structural uncertainty without perturbing structural observations and can help target locations for additional data collection. Variability in the interpolated models is compared using information entropy on the resulting scalar field as well as a new metric to classify the geometrical variability between models. The combination of a local quantification of model uncertainty and the posterior distributions for the fold geometry parameters can be used to reduce overall model variability. In a synthetic case study the model variability is reduced by up to 60% after adding data characterising a single parasitic fold hinge. These methods could be incorporated into geological exploration where the highest variability locations can be used as a target locations for further data collection (e.g. field mapping and/or drilling).

Acknowledgements

This research was partially funded by Australian Research Council Linkage grant LP140100267, and partly supported by the "Investissements d'avenir" Labex RESSOURCES21 (ANR-10-LABX-21-01). The authors are grateful to the industrial and academic sponsors of the Gocad Research Consortium managed by ASGA (Association Scientifique pour la Géologie et ses Applications, http://ring.georessources.univ-lorraine.fr/) for their support. We thank Paradigm for providing the GOCAD-SKUA software and API. The final case study in this publication was generated with the StructuralFactory plugin for Gocad, based on RING's StructuralLab plugin. Reviews by Florian Wellmann and Ernst Schetselaar significantly improved the quality of the manuscript. Last but not least, the authors would like to thank Guillaume Caumon and Paul Cupillard for their feedback and discussions. Supplementary data for the final case study and the noddy history file can be accessed from: https://figshare.com/s/03cdb58d7727aad73daf. Code used for the 1-D examples can be accessed on from https://github.com/lachlangrose/grose2018_jgr_structural_inversion/

References

Armit, R. J., P. G. Betts, B. F. Schaefer, and L. Ailleres (2012), Constraints on long-lived Mesoproterozoic and Palaeozoic deformational events and crustal architecture in the northern Mount Painter Province, Australia, *Gondwana Research*, *22*(1), 207–226, doi:10.1016/j.gr.2011.11.003. *(Cited page 10)*

Aug, C., J.-P. Chilès, G. Courrioux, and C. Lajaunie (2005), 3D Geological Modelling and Uncertainty: The Potential-field Method, in *Geostatistics Banff 2004*, vol. 31, edited by O. Leuangthong and C. Deutsch, pp. 145–154, Springer Netherlands, doi:10.1007/978-1-4020-3610-1{_}15. *(Cited pages 1 and 12)*

Aydin, O., and J. K. Caers (2017), Quantifying structural uncertainty on fault networks using a marked point process within a Bayesian framework, *Tectonophysics*, *712-713*, 101–124, doi:10.1016/j.tecto.2017.04.027. *(Cited page 9)*

Bárdossy, G., and J. Fodor (2001), Traditional and new ways to handle uncertainty in geology, *Natural Resources Research*, *10*(3). *(Cited page 4)*

Basson, I., P. Creus, C. Anthonissen, B. Stoch, and J. Ekkerd (2016), Structural analysis and implicit 3D modelling of high-grade host rocks to the Venetia kimberlite diatremes, Central Zone, Limpopo Belt, South Africa, *Journal of Structural Geology*, *86*, 47–61, doi:10.1016/j.jsg.2016.03.002. *(Cited page 10)*

Bigi, S., A. Conti, P. Casero, L. Ruggiero, R. Recanati, and L. Lipparini (2013), Geological model of the central Periadriatic basin (Apennines, Italy), *Marine and Petroleum Geology*, *42*, 107–121, doi:10.1016/j.marpetgeo.2012.07.005. *(Cited page 1)*

Bodin, T., M. Sambridge, N. Rawlinson, and P. Arroucau (2012a), Transdimensional tomography with unknown data noise, *Geophysical Journal International*, *189*(3), 1536–1556, doi:10.1111/j.1365-246X.2012.05414.x. *(Cited page 4)*

Bodin, T., M. Sambridge, H. Tkalćić, P. Arroucau, K. Gallagher, and N. Rawlinson (2012b), Transdimensional inversion of receiver functions and surface wave dispersion, *Journal of Geophysical Research: Solid Earth*, *117*(2), 1–25, doi:10.1029/2011JB008560. *(Cited page 4)*

Bond, C. E., A. D. Gibbs, Z. K. Shipton, and S. Jones (2007), What do you think this is? "Conceptual uncertainty" In geoscience interpretation, *GSA Today*, *17*(11), 4–10, doi:10.1130/GSAT01711A.1. *(Cited page 12)*

Cauchy, A. (1847), Méthode générale pour la résolution des systemes d'équations simultanées, *Comp. Rend. Sci. Paris*, (2), 2–4. *(Cited page 5)*

Caumon, G., P. Collon-Drouaillet, C. Le Carlier de Veslud, S. Viseur, and J. Sausse (2009), Surface-Based 3D Modeling of Geological Structures, *Mathematical Geosciences*, *41*(8), 927–945, doi:10.1007/s11004-009-9244-2. *(Cited pages 1 and 12)*

Caumon, G., G. Gray, C. Antoine, and M.-O. Titeux (2013), Three-Dimensional Implicit Stratigraphic Model Building From Remote Sensing Data on Tetrahedral Meshes: Theory and Application to a Regional Model of La Popa Basin, NE Mexico, *IEEE Transactions on Geoscience and*

Remote Sensing, *51*(3), 1613–1621, doi:10.1109/TGRS.2012.2207727. *(Cited page 1)*

Cherpeau, N., G. Caumon, and B. Lévy (2010), Stochastic simulations of fault networks in 3D structural modeling, *Comptes Rendus Geoscience*, *342*(9), 687–694, doi:10.1016/j.crte.2010.04.008. *(Cited page 11)*

Cherpeau, N., G. Caumon, J. Caers, and B. Lévy (2012), Method for Stochastic Inverse Modeling of Fault Geometry and Connectivity Using Flow Data, *Mathematical Geosciences*, *44*(2), 147–168, doi:10.1007/s11004-012-9389-2. *(Cited page 11)*

Collon, P., A. Pichat, C. Kergaravat, A. Botella, G. Caumon, J.-C. Ringenbach, and J.-P. Callot (2016), 3D modeling from outcrop data in a salt tectonic context: Example from the Inceyol minibasin, Sivas Basin, Turkey, *Interpretation*, *4*(3), SM17–SM31, doi:10.1190/INT-2015-0178.1. *(Cited page 8)*

Cowan, E., R. Beatson, H. Ross, W. Fright, T. McLennan, T. Evans, J. Carr, R. Lane, D. Bright, A. Gillman, P. Oshust, and M. Titley (2003), Practical implicit geological modelling, *5th International Mining Geology Conference*, (8), 89–99. *(Cited page 1)*

Cox, L. A. (1982), Artifactual Uncertainty in Risk Analysis, *Risk Analysis*, *2*, 121–135. *(Cited page 4)*

de la Varga, M., and J. F. Wellmann (2016), Structural geologic modeling as an inference problem: A Bayesian perspective, *Interpretation*, *4*(3), 1–16, doi:10.1190/INT-2015-0188.1. *(Cited pages 4, 9, 10, 11, and 12)*

Forbes, C. J., and P. G. Betts (2004), Development of Type 2 fold interference patterns in the Broken Hill Block: implications for strain partitioning across a detachment during the Olarian Orogeny, *Australian Journal of Earth Sciences*, *51*(2), 173–188, doi:10.1111/j.1440-0952.2004.01051.x. *(Cited page 10)*

Frank, T., A.-L. Tertois, and J.-L. Mallet (2007), 3D-reconstruction of complex geological interfaces from irregularly distributed and noisy point data, *Computers & Geosciences*, *33*(7), 932–943, doi:10.1016/j.cageo.2006.11.014. *(Cited pages 1 and 8)*

Frehner, M., and S. M. Schmalholz (2006), Numerical simulations of parasitic folding in multilayers, *Journal of Structural Geology*, *28*, 1647–1657, doi:10.1016/j.jsg.2006.05.008. *(Cited page 3)*

Gelman, A., A. Jakulin, M. G. Pittau, and Y. S. Su (2008), A weakly informative default prior distribution for logistic and other regression models, *Annals of Applied Statistics*, *2*(4), 1360–1383, doi:10.1214/08-AOAS191. *(Cited page 4)*

Grose, L., G. Laurent, L. Aillères, R. Armit, M. Jessell, and G. Caumon (2017), Structural data constraints for implicit modeling of folds, *Journal of Structural Geology*, *104*, 80–92, doi:10.1016/j.jsg.2017.09.013. *(Cited pages 2, 3, 4, 5, 7, 9, and 12)*

Hillier, M. J., E. M. Schetselaar, E. A. de Kemp, and G. Perron (2014), Three-Dimensional Modelling of Geological Surfaces Using Generalized Interpolation with Radial Basis Functions, *Mathematical Geosciences*, *46*(8), 931–953, doi:10.1007/s11004-014-9540-3. *(Cited pages 1 and 8)*

Jessell, M., L. Aillères, E. D. Kemp, M. Lindsay, F. Wellmann, M. Hillier, G. Laurent, T. Carmichael, and R. Martin (2014), Next generation 3D geological modelling and inversion, in *Society of Economic Geologists Special Publication 18*, chap. 13, pp. 261–272. *(Cited pages 1 and 12)*

Jessell, M. W., and R. K. Valenta (1996), Structural geophysics: Integrated structural and geophysical modelling, *Computer Methods in the Geosciences*, *15*, 303–324, doi:10.1016/S1874-561X(96)80027-7. *(Cited pages 1 and 6)*

Jessell, M. W., L. Ailleres, and E. A. de Kemp (2010), Towards an integrated inversion of geoscientific data: What price of geology?, *Tectonophysics*, *490*(3-4), 294–306, doi:10.1016/j.tecto.2010.05.020. *(Cited pages 1, 2, and 11)*

Kolb, J. M., and V. Lekić (2014), Receiver function deconvolution using transdimensional hierarchical bayesian inference, *Geophysical Journal International*, *197*(3), 1719–1735, doi:10.1093/gji/ggu079. *(Cited page 4)*

Lajaunie, C., G. Courrioux, and L. Manuel (1997), Foliation fields and 3D cartography in geology: Principles of a method based on potential interpolation, *Mathematical Geology*, *29*(4), 571–584, doi:10.1007/BF02775087. *(Cited page 1)*

Laurent, G., G. Caumon, A. Bouziat, and M. Jessell (2013), A parametric method to model 3D displacements around faults with volumetric vector fields, *Tectonophysics*, *590*, 83–93, doi:10.1016/j.tecto.2013.01.015. *(Cited page 1)*

Laurent, G., L. Ailleres, L. Grose, G. Caumon, M. Jessell, and R. Armit (2016), Implicit modeling of folds and overprinting deformation, *Earth and Planetary Science Letters*, *456*, 26–38, doi:10.1016/j.epsl.2016.09.040. *(Cited pages 1, 2, 3, 5, 7, and 12)*

Lindsay, M. D., L. Aillères, M. W. Jessell, E. A. de Kemp, and P. G. Betts (2012), Locating and quantifying geological uncertainty in three-dimensional models: Analysis of the Gippsland Basin, southeastern Australia, *Tectonophysics*, *546-547*, 10–27, doi:10.1016/j.tecto.2012.04.007. *(Cited pages 2, 4, 7, 11, and 12)*

Lindsay, M. D., S. Perrouty, M. W. Jessell, and L. Ailleres (2013), Making the link between geological and geophysical uncertainty: geodiversity in the Ashanti Greenstone Belt, *Geophysical Journal International*, *195*(2), 903–922, doi:10.1093/gji/ggt311. *(Cited page 11)*

Mallet, J.-L. (1992), Discrete smooth interpolation in geometric modelling, *Computer-Aided Design*, *24*(4), 178–191, doi:10.1016/0010-4485(92)90054-E. *(Cited page 1)*

Mallet, J.-l. (2002), *Geomodeling*, Oxford University Press, New York, NY, USA. *(Cited page 1)*

Mann, J. C. (1993), Uncertainty in Geology, in *Computers in geology– 25 years of progress*, pp. 241–254, Oxford University Press, New York, NY, USA. *(Cited page 4)*

Maxelon, M., P. Renard, G. Courrioux, M. Brändli, and N. Manckтelow (2009), A workflow to facilitate three-dimensional geometrical modelling of complex poly-deformed geological units, *Computers & Geosciences*, *35*(3), 644–658, doi:10.1016/j.cageo.2008.06.005. *(Cited pages 1 and 10)*

Moretti, I. (2008), Working in complex areas: New restoration workflow based on quality control, 2D and 3D restorations, *Marine and Petroleum Geology*, *25*(3), 205–218, doi:10.1016/j.marpetgeo.2007.07.001. *(Cited page 1)*

Mosegaard, K., and A. Tarantola (1995), Monte Carlo sampling of solutions to inverse problems, *Journal of Geophysical Research*, *100*(B7), 12,431–12,447, doi:10.1029/94JB03097. *(Cited pages 2 and 4)*

Muir, J., and H. Tkalčić (2015), A method of spherical harmonic analysis in the geosciences via hierarchical Bayesian inference, *Geophysical Journal International*, *203*(2), 1164–1171, doi:10.1093/gji/ggv361. *(Cited page 4)*

Patil, A., D. Huard, and C. J. Fonnesbeck (2010), PyMC: Bayesian Stochastic Modelling in Python., *Journal of statistical software*, *35*(4), 1–81, doi:10.18637/jss.v035.i04. *(Cited page 5)*

Raftery, A. E. (1996), Approximate Bayes Factors and Accounting for Model Uncertainty in Generalised Linear Models, *Biometrika*, *83*(2), 251–266. *(Cited page 4)*

Ramsay, J. G., and M. I. Huber (1987), *The techniques of modern structural geology, Volume 2: Folds and fractures*, London ; New York: Academic Press. *(Cited page 3)*

Sivia, D. S. (1996), *Data analysis : a Bayesian tutorial*, Oxford : Clarendon Press, Oxford : New York. *(Cited pages 4 and 5)*

Suzuki, S., G. Caumon, and J. Caers (2008), Dynamic data integration for structural modeling: model screening approach using a distance-based model parameterization, *Computational Geosciences*, *12*(1), 105–119, doi:10.1007/s10596-007-9063-9. *(Cited pages 2 and 11)*

Tacher, L., I. Pomian-Srzednicki, and A. Parriaux (2006), Geological uncertainties associated with 3-D subsurface models, *Computers & Geosciences*, *32*(2), 212–221, doi:10.1016/j.cageo.2005.06.010. *(Cited page 2)*

Thiele, S. T., M. W. Jessell, M. Lindsay, J. F. Wellmann, and E. Pakyuz-Charrier (2016), The topology of geology 2: Topological uncertainty, *Journal of Structural Geology*, *91*, 74–87, doi:10.1016/j.jsg.2016.08.010. *(Cited page 11)*

Thore, P., A. Shtuka, M. Lecour, T. AitEttajer, and R. Cognot (2002), Structural uncertainties: Determination, management, and applications, *Geophysics*, *67*(3), 840–852, doi:10.1190/1.1484528. *(Cited page 2)*

Tian, Z., J. Sun, B. F. Windley, Z. Zhang, Z. Gong, X. Lin, and W. Xiao (2016), Cenozoic detachment folding in the southern Tianshan foreland, NW China: Shortening distances and rates, *Journal of Structural Geology*, *84*, 142–161, doi:10.1016/j.jsg.2016.01.007. *(Cited page 10)*

Twiss, R. J. (1992), *Structural geology*, W.H. Freeman, New York. *(Cited page 3)*

Vollgger, S. A., A. R. Cruden, L. Ailleres, and E. J. Cowan (2015), Regional dome evolution and its control on ore-grade distribution: Insights from 3D implicit modelling of the Navachab gold deposit, Namibia, *Ore Geology Reviews*, *69*, 268–284, doi:10.1016/j.oregeorev.2015.02.020. *(Cited page 10)*

Wellmann, J. F., and K. Regenauer-Lieb (2012), Uncertainties have a meaning: Information entropy as a quality measure for 3-D geological models, *Tectonophysics*, *526-529*, 207–216, doi:10.1016/j.tecto.2011.05.001. *(Cited pages 2, 4, 7, 11, and 12)*

Wellmann, J. F., F. G. Horowitz, E. Schill, and K. Regenauer-Lieb (2010), Towards incorporating uncertainty of structural data in 3D geological

inversion, *Tectonophysics*, *490*(3-4), 141–151, doi:10.1016/j.tecto.2010.04.022. *(Cited pages 4, 7, 11, and 12)*

Wellmann, J. F., S. T. Thiele, M. D. Lindsay, M. W. Jessell, and J. Abc (2016), pynoddy 1.0 : an experimental platform for automated 3-D kinematic and potential field modelling, *Geoscientific Model Development*, pp. 1019–1035, doi:10.5194/gmd-9-1019-2016. *(Cited page 6)*

Wellmann, J. F., M. D. E. L. A. Varga, R. E. Murdie, K. Gessner, M. Jessell, M. de la Varga, R. E. Murdie, K. Gessner, and M. Jessell (2017), Uncertainty estimation for a geological model of the Sandstone greenstone belt, Western Australia {\textendash} insights from integrated geological and geophysical inversion in a Bayesian inference framework, *Geological Society, London, Special Publications*, *453*, doi:10.1144/SP453.12. *(Cited page 9)*

Wood, R., and A. Curtis (2004), Geological prior information and its applications to geoscientific problems, *Geological Society, London, Special Publications*, *239*(1), 1–14, doi:10.1144/GSL.SP.2004.239.01.01. *(Cited page 9)*